

# Joint Research Highlights

## Thermal-Hall effect in a Spin-Liquid State in Volborthite

M. Yamashita, T. Shibauchi, and Y. Matsuda

A central question in condensed-matter physics is a fate of electronic states under strong quantum fluctuations which often give rise to a variety of non-trivial quantum states. A prominent example is a quantum spin liquid (QSL) [1] of frustrated quantum antiferromagnets in which highly-correlated spins keep fluctuating down to very low temperature owing to enhanced quantum fluctuations. A few candidate materials now have been reported to host a QSL in two-dimension (2D), which have been attracting enormous attention because a 2D QSL is a new class of matter characterized by unknown quasiparticles. Identifying the precise nature of elementary excitations in a 2D QSL, however, has remained entirely elusive.

To shed a new light for studying unexplored property of the elementary excitations in a QSL, we utilize thermal Hall measurements to a spin liquid state realized in a 2D kagomé insulator volborthite  $\text{Cu}_3\text{V}_2\text{O}_7(\text{OH})_2 \cdot 2\text{H}_2\text{O}$ . Volborthite is a magnetic insulator in which  $\text{Cu}^{2+}$  ions form a distorted kagomé structure with inequivalent exchange interactions [2] (see the inset of Fig. 1). The temperature dependence of the magnetic susceptibility  $\chi$  is typical for frustrated spin system with the effective spin interaction energy  $J_{\text{eff}}/k_B \sim 60$  K; the peak of  $\chi(T)$  at  $T_p \sim 18$  K shows that a short-range spin correlation develops below  $T_p$ . Although the spin Hamiltonian is rather complicated [3], a geometrical

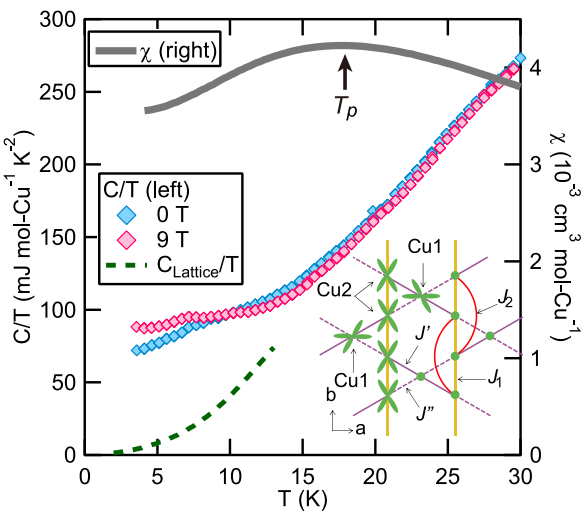


Fig. 1. Temperature dependence of the heat capacity divided by temperature  $C/T$  (diamonds, left axis) and the magnetic susceptibility  $\chi$  (gray line, right axis) of a single crystal of volborthite. The peak temperature of the magnetic susceptibility is marked as  $T_p$ . The dashed line is the lattice heat capacity. The inset illustrates the arrangement of Cu ions in the  $ab$  plane.  $J_1$  and  $J_2$  represent the nearest-neighbor and next-nearest-neighbor interactions in the Cu2 spin chains, respectively.  $J'$  and  $J''$  represent the nearest-neighbor interactions between Cu1 and Cu2 spins.

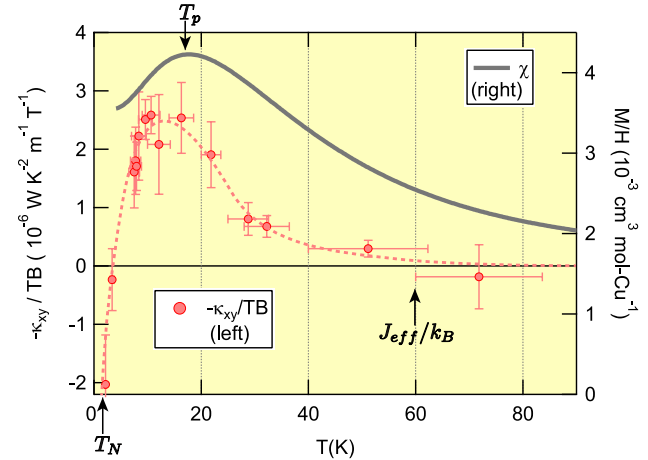


Fig. 2. Temperature dependence of  $-\kappa_{xy}/TB$  at 15 T (left) and that of  $\chi$  (right). The dashed line is a guide to the eyes.

frustration effect suppressed the magnetic order down to  $T_N \sim 1$  K, showing a presence of a spin liquid state in a wide temperature range  $T_N < T < J_{\text{eff}}/k_B$ . Extrapolating both  $\chi$  and  $C/T$  above  $T_N$  results a finite value at  $T = 0$  (Fig. 1), demonstrating the presence of gapless excitations in the spin liquid state.

Our central finding [4] is a negative thermal Hall conductivity  $\kappa_{xy}$  (Fig. 2) which develops upon entering the spin liquid state ( $T < J_{\text{eff}}/k_B$ ) from the high-temperature paramagnetic state ( $T > J_{\text{eff}}/k_B$ ). Because volborthite is a transparent insulator without conducting electrons, a finite thermal Hall effect immediately means the presence of non-trivial excitations. At lower temperatures,  $|\kappa_{xy}|$  shows a peak at  $T \sim T_p$ , which is followed by a sharp decrease and a sign inversion just above  $T_N$ . These intimate correlations between the temperature dependence of  $\chi$  and that of  $\kappa_{xy}$  lead us to conclude that the observed thermal Hall effect in volborthite arises from the magnetic excitations in the spin liquid state, not from phonons. The emergence of the thermal Hall conductivity below  $T \sim J_{\text{eff}}/k_B$  strongly suggests that the thermal Hall effect is a key signature distinguishing the highly-correlated spin liquid state from the conventional paramagnetic state. A further analysis [4] shows that an effective Lorentz force acting on the spin excitations can be estimated as  $\sim 1/100$  of that for free electrons, implying that the coupling between the applied magnetic field and the spin excitations is very small.

The rapid decrease and the sign change of  $\kappa_{xy}$  near  $T_N$  call further studies, especially about the spin correlation effect on the thermal Hall conductivity. Possibilities for the suppression of  $\kappa_{xy}$  would include an instability of a fictitious gauge field acting on the spin excitations and an emergence of an additional spin excitations with opposite sign of  $\kappa_{xy}$ . Applying thermal Hall measurements to another frustrated spin materials should be important to clarify these nontrivial issues.

## References

- [1] L. Balents, *Nature* **464**, 199 (2010).
- [2] H. Ishikawa *et al.*, *Phys. Rev. Lett.* **114**, 227202 (2015).
- [3] O. Janson *et al.*, *Phys. Rev. Lett.* **117**, 037206 (2016).
- [4] D. Watanabe *et al.*, *Proc. Natl. Acad. Sci. USA* **113**, 8653 (2016).

## Authors

- D. Watanabe<sup>a</sup>, K. Sugii, M. Shimozawa, Y. Suzuki, T. Yajima, H. Ishikawa, Z. Hiroi, T. Shibauchi<sup>b</sup>, Y. Matsuda<sup>a</sup>, and M. Yamashita<sup>a</sup>  
<sup>a</sup>Kyoto University.  
<sup>b</sup>University of Tokyo

## Spin Control in Photoemission Process from Spin-Orbital Entangled Surface States

K. Kobayashi, F. Komori, and S. Shin

Strongly spin-orbit coupled materials have been attracting much attention in solid-state physics. In particular, the potential gradient at the surface and interface largely enhances the interaction. In contrast to a conventional model with a single chiral spin texture of spin-polarized surface states, the spin-orbital texture, where spin is locked to the orbital texture of the bands, has recently been pointed out. [1] The spin-orbital entanglement is a general consequence of the strong spin-orbit coupling, and thus is important not only for surface/interface states but also bulk states, and is applicable to optical spin control in solids. However, the response of spin to light has not yet been understood fully on the basis of the quantum-mechanically entangled states with spin-orbital textures. Consequently, a clear and comprehensive concept is required on this subject. We have shown general description of the optical spin control using the spin-orbital entangled states, and demonstrated it in  $\text{Bi}_2\text{Se}_3$  [2], and Bi [3] surfaces by laser-based spin- and angle-resolved photoemission spectroscopy (Laser-SARPES) [4].

In the preset concept, the final state spin direction of photo-excited electrons is determined by quantum interference due to spin-locked wave functions in the optical excitation process as schematically shown in Fig.1. On the mirror symmetry line, the spin direction of the initial state is fixed by the even-odd symmetry of the orbital wave function. In the case of SARPES measurements on the mirror symmetry line, spin direction of the photoelectron excited by linearly-polarized light depends systematically on the direction of its electric field vector, and can be expressed by the light-polarization angle ( $\theta$ ) from the mirror plane and a complex

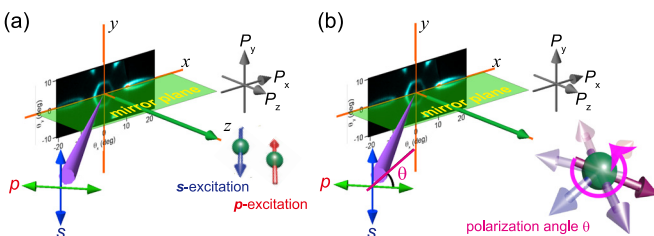


Fig. 1. Schematic illustration of photoemission processes from spin-orbital entangled surface states, where spin direction is locked in either  $y$  or  $-y$  direction, depending on the even-odd symmetry of the orbital wave functions and mirror-symmetry eigen values on the mirror-symmetry line. When the surface is irradiated by  $p(s)$ -polarized light in the mirror plane, only even(odd)-symmetry wave functions are excited, and thus, the spin direction of photoelectrons is either  $y$  or  $-y$  direction accordingly as shown in (a). When the electric field direction of light is rotated by  $\theta$  from the  $p$ -polarization direction as in (b), both even and odd wave functions are coherently excited and the spin direction of the photoelectrons is determined by complex matrix elements of the photo-excitation process [2,3].

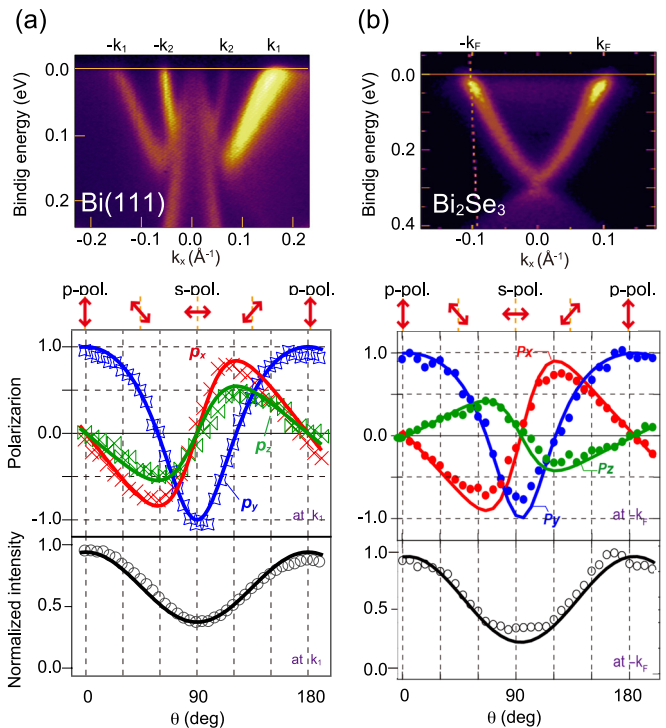


Fig. 2. ARPES of spin-orbital entangled surface states (upper), and photoelectron spin direction (middle) and normalized photoelectron intensity (lower) as a function of the angle  $\theta$  of the polarization vector from the  $p$ -polarization direction shown in Fig.1(b) for the  $\text{Bi}(111)$  (a) [3] and  $\text{Bi}_2\text{Se}_3(111)$  (b) [2] surfaces. For  $\text{Bi}(111)$ , two surface bands exist around  $\Gamma$  while only one band for  $\text{Bi}_2\text{Se}_3(111)$ . Initial states of the photoelectrons are at  $k_1$  and  $E_F$  for (a), and  $-k_F$  for (b). The observed  $\theta$  dependences are well reproduced by the formula (solid curves) using two fitting parameters of the photoemission matrix element ratio.

ratio of the dipole matrix elements from the even and odd initial states. We measured the spin direction of photoelectrons from  $\text{Bi}_2\text{Se}_3(111)$  and  $\text{Bi}(111)$  surfaces as a function of  $\theta$  using Laser-SARPES. The results are well reproduced by the obtained formula as shown in Fig. 2 using appropriate complex values of the matrix element ratio.

## References

- 1. Z.-H. Zhu *et. al.*, *Phys. Rev. Lett* **110**, 216401 (2013).
- 2. K. Kuroda *et. al.*, *Phys. Rev. B* **94**, 165162 (2016).
- 3. K. Yaji *et. al.*, *Nat. Commun.* **8**, 14588 (2017).
- 4. K. Yaji *et. al.*, *Rev. Sci. Instrum.* **87**, 053111 (2016).

## Authors

- K. Yaji, K. Kuroda, K. Kobayashi<sup>a</sup>, A. Harasawa, Y. Ishida, S. Watanabe, C. Chen<sup>c</sup>, F. Komori, and S. Shin  
<sup>a</sup>Ochanomizu University  
<sup>b</sup>Research Institute for Science and Technology, Tokyo University of Science  
<sup>c</sup>Beijing Center for Crystal Research and Development, Chinese Academy of Science

## Compressed Sensing in Scanning Tunneling Microscopy/Spectroscopy for Quasi-Particle Interference

Y. Nakanishi-Ohno, Y. Yoshida, and M. Okada

Interference of electrons is one of the manifestations of their particle-wave duality in quantum mechanics. When electrons are scattered by local disordered structures, such as adsorbates and step edges on surfaces, the reflected electronic wave interferes with the injected one to form a spatial modulation in local density of states (LDOS), that is,

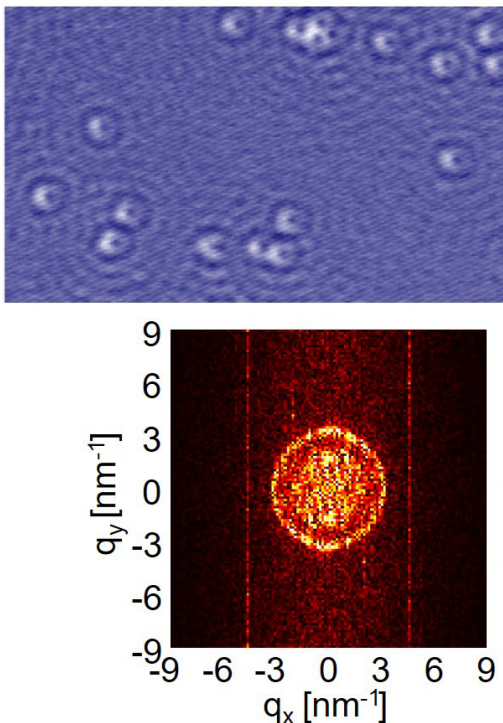


Fig. 1. (upper)  $dI/dV$  map taken on the Ag(111) surface. The size of the area is  $70 \text{ nm} \times 35 \text{ nm}$ , and the number of pixels is  $360 \times 180 = 64800$  points. (lower) FT of the upper STM image by the conventional method.

a quasi-particle interference (QPI) pattern. The modulated LDOS can be observed in real space by using scanning tunneling microscopy and spectroscopy (STM/S) at various energies around the Fermi level, and by analyzing a QPI pattern one can obtain the momentum ( $k$ ) space information on the electronic states and their energy dispersion relation. Recently, the QPI analysis has been applied to investigate electronic structures of complex materials such as unconventional superconductors and topological insulators. As the measurements can be performed at very low temperature under high magnetic fields, the method is a powerful tool in various aspects of solid state physics.

In order to obtain the energy dispersion relation of electronic states, however, the spectrum of tunneling conductance  $dI/dV$ , which corresponds to LDOS, has to be taken at every pixel while scanning. It is therefore quite time-consuming; sometimes it takes more than a week, which makes the QPI measurements difficult to be performed. If one can obtain the same quality of the  $k$ -space information from a reduced number of spectra, the QPI analysis will be much more convenient and widely used.

As a solution to the problem posed above, we have applied compressed sensing (CS) to the QPI observation, which is a novel statistical method for acquiring and reconstructing a signal efficiently. In the case of QPI observation, the  $k$ -space information on the electronic states is obtained by performing the Fourier transformation (FT) of the QPI pattern. If the number of  $dI/dV$  spectra is decreased, the FT of the  $dI/dV$  map becomes of too low quality to access the  $k$ -space information. In order to boldly enhance the resolution of  $k$  space, we need to solve an underdetermined problem, in which the number of variables measured is smaller than the number of variables to be determined. CS addresses this problem by utilizing the sparseness of QPI patterns; their FTs are composed of few nonzeros and many zeros. This sparseness is based on the fact that LDOS modulations are allowed only for a small number of

wavelengths. Because of this sparseness, we can reduce the number of unknown variables significantly, and then obtain an FT of sufficient quality even with scarce data.

Here, we demonstrate that CS performs well by numerical simulations on a QPI pattern observed in a  $dI/dV$  map of the Ag(111) surface. The surface state of Ag(111) is described by a free-electron-like model, and the FT of the QPI pattern has a circular pattern whose radius corresponds to twice the wavenumber of the states. We use an analysis method of CS, called LASSO (least absolute shrinkage and selection operator), to recover the pattern from scarce data.

Figure 1 shows a  $dI/dV$  mapping ( $360 \times 180 = 64800$  pixels) taken on the Ag(111) surface at 4.2 K. The mapping shows a wave-like QPI pattern around adsorbates on the surface. The FT of this  $dI/dV$  map obtained by the conventional method is shown in the lower panel of Fig. 1. A ring structure can be seen centered at the origin, indicating the presence of isotropic electronic states on the surface. We also found small intensity other than the ring, supporting the assumption of sparseness. The  $q$ -space region of interest is discretized into  $128 \times 128 = 16384$  pixels. In this case, the amount of data is enough sufficient compared to the number of unknown variables.

Let us examine whether the circle can be recovered from a reduced amount of data. Figure 2 shows FTs of 16384 pixels, which are estimated from data of 7200 points randomly chosen from the  $dI/dV$  mapping shown in Fig. 1. It should be noted that the number of unknown variables is larger than that of the measured variables. The left and right panels show the results of the conventional method and those of LASSO, respectively. Although the ring pattern can be seen in the FT by the conventional process (left panel), it has rather noisy background because of the reduced amount of data. On the other hand, the analysis with LASSO significantly reduces the background noise, and the expected pattern is more clearly seen in the result (right panel). In the ill-posed situation, LASSO provides a sparse solution; most of the noise components are automatically estimated at zero, and the signal components remain to be nonzero. Our numerical simulations demonstrated that LASSO enables us to recover the characteristic features of the electronic states of Ag(111) surface from a randomly reduced dataset. Our results indicate that CS works effectively in the analysis of QPI, saving the number of required dataset and measurement time, which improve the efficiency of the QPI analysis. Obviously the application of CS should not be limited to the QPI analysis; we expect that it will be extended more to various situations in condensed matter physics near future.

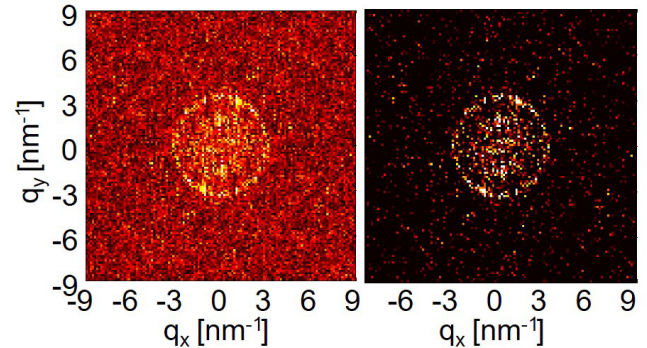


Fig. 2. FTs estimated from pixels randomly chosen from the  $dI/dV$  mapping shown in the upper panel of Fig. 1. The subsets of data are composed of 7200 pixels. Results of the conventional method and LASSO are shown in the left and right panels, respectively.

## Reference

[1] Y. Nakanishi-Ohno, M. Haze, Y. Yoshida, K. Fukushima, Y. Hasegawa, and M. Okada, J. Phys. Soc. Jpn. **85**, 093702 (2016).

## Authors

Y. Nakanishi-Ohno<sup>a</sup>, M. Haze, Y. Yoshida, K. Fukushima<sup>a,b</sup>, Y. Hasegawa, and M. Okada<sup>a</sup>

<sup>a</sup>The University of Tokyo

<sup>b</sup>National Institute for Materials Science

## Halide Perovskite Thin Films for Photovoltaics

K. Kawashima, R. Takahashi, and M. Lippmaa

Structurally similar to classical perovskite oxides, organic halide perovskites have a general formula  $ABX_3$ , where the anion X can be I, Br, or Cl, the B-site is occupied by Pb, and the A-site usually holds the methylammonium ion,  $\text{CH}_3\text{NH}_3^+$ . Halide perovskites are studied as energy harvesting materials in photovoltaics, achieving solar cell energy conversion efficiencies of around 20%. A major technical problem with perovskite solar cells is the low structural stability of the halide perovskite material. The carrier mobility and recombination rates therefore quickly degrade after film growth. The purpose of this collaboration project was to develop a technique for quickly fabricating organic halide perovskite thin films with controlled composition and layer thickness to optimize the material characteristics. A pulsed molecular beam epitaxy system with continuous wave infrared heating (cwIR-MBE) was designed to tackle this problem. The thin film growth system is shown in Fig. 1a, showing two precursor cells containing the  $\text{PbI}_2$  and  $\text{CH}_3\text{NH}_3\text{I}$  precursors on a rotatable target stage. The stage can be used to position either one of the sources to face directly the substrate. A cw infrared laser is used to briefly heat the source cell in front of the substrate, yielding a millisecond-scale pulsed MBE process. The amount of material evaporated can be controlled by tuning the laser power, pulse length, and the evaporation pulse count. The main benefit of the technique is that the evaporation is thermal, not ablative, which means that the organic precursor material is not decomposed in the evaporation process. Periodically evaporating either of the two sources is used to obtain the desired  $\text{PbI}_2$  and  $\text{CH}_3\text{NH}_3\text{I}$  layer sequence. A homogeneous perovskite phase can be obtained if the individual layer thicknesses are limited to just a few unit cells and the average stoichiometry is close to the desired value.

This thin film growth system was used to fabricate arrays of perovskite solar cells, integrating several devices with slightly different precursor ratios on a single substrate to

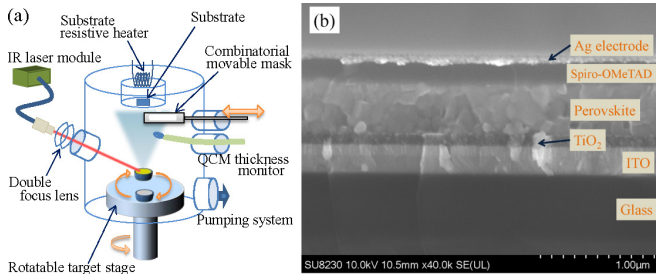


Fig. 1. (a) Schematic view of the pulse MBE deposition system. (b) A cross-sectional image of a completed organic halide perovskite solar cell.

minimize statistical errors in the device characterization. A cross-sectional view of a completed solar cell device is shown in Fig. 1b. X-ray diffraction analysis was used to determine the optimal evaporated precursor ratio to obtain the perovskite phase. The total film thickness analysis was used to confirm that homogeneous phase formation occurs in multilayer films where the  $\text{PbI}_2$  and  $\text{CH}_3\text{NH}_3\text{I}$  layer thicknesses are 1.4 nm and 1.7 nm, respectively. Characterizing a series of solar cells showed that even in the screening experiment, a device efficiency of 10 % could be achieved.

The success of the halide perovskite synthesis by IR-MBE shows that sequential evaporation of organic precursor sources is an effective way of depositing nanometer-scale layers of volatile organics in a physical vapor vacuum process. The geometry of the evaporation process is arranged so that each target is directly facing the substrate during evaporation, which minimizes spatial layer thickness gradients on the sample surface. Additionally, only a single laser is required to evaporate several different precursor materials, while the necessary heating power and pulse length can be adjusted individually for each precursor material. The work thus shows that organic multilayer and homogeneous phase materials can be grown in a technically simple sequential MBE chamber.

## References

[1] K. Kawashima, Y. Okamoto, O. Annayev, N. Toyokura, R. Takahashi, M. Lippmaa, K. Itaka, Y. Suzuki, N. Matsuki, and H. Koinuma, Sci. Tech. Adv. Mat. **18**, 307 (2017).

## Authors

K. Kawashima<sup>a</sup>, Y. Okamoto<sup>b</sup>, O. Annayev<sup>c</sup>, N. Toyokura<sup>a</sup>, R. Takahashi<sup>d</sup>, M. Lippmaa<sup>b</sup>, K. Itaka<sup>d</sup>, Y. Suzuki<sup>b</sup>, N. Matsuki<sup>e</sup>, and H. Koinuma<sup>f</sup>

<sup>a</sup>Comet Co. Ltd.

<sup>b</sup>Tsukuba University

<sup>c</sup>Turkmenistan Academy of Science and Technology

<sup>d</sup>Hiroaki University

<sup>e</sup>Kanagawa University

<sup>f</sup>National Institute for Materials Science

## Pressure Effect on Magnetic Properties of Weak Itinerant Electron Ferromagnet CrAlGe

Y. Mitsui, Y. Uwatoko, and K. Koyama

CrAlGe with an orthorhombic  $\text{TiSi}_2$ -type structure shows ferromagnetism below a Curie temperature  $T_C$  of 80 K. The spontaneous magnetic moment  $p_s$  and effective magnetic moment  $p_{\text{eff}}$  of CrAlGe were reported to be 0.41  $\mu_B$  at 5 K and 1.89  $\mu_B$ , respectively [1]. The paramagnetic moment  $p_C$  was calculated to be 1.13  $\mu_B$  from  $p_{\text{eff}}$  by  $p_{\text{eff}}^2 = p_C(p_C + 2)$ , and the ratio  $p_C/p_s$  of CrAlGe was 2.8. Because the  $p_C/p_s$  is greater than unity, CrAlGe was classified as the weak itinerant electron ferromagnet (WIEF). The parameters of the energy scale of the spin fluctuation spectrum [2],  $T_0$  and  $T_A$  were estimated to be  $1.0 \times 10^3$  K and  $4.0 \times 10^3$  K, respectively. However, the pressure effect on the magnetic properties of CrAlGe has not been clarified. In this study, we performed magnetization measurements of CrAlGe under high pressures up to 1 GPa.

The magnetization  $M$  measurements under hydrostatic pressure  $P$  up to 1.0 GPa were carried out using a superconducting quantum interference device magnetometer for  $5 \leq T \leq 200$  K and magnetic fields  $\mu_0 H$  up to 5 T in a clamp-

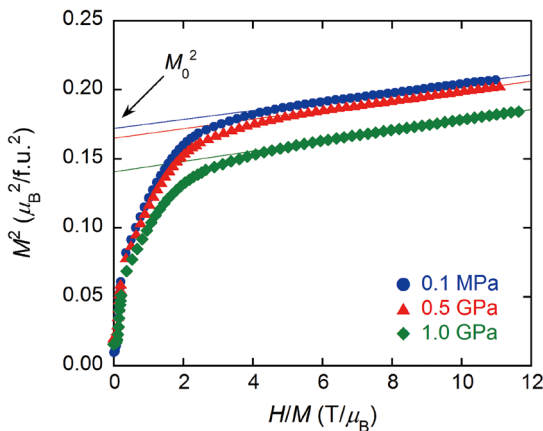


Fig. 1. Isothermal  $M^2$  vs.  $H/M$  plots (Arrott plots) of CrAlGe under several pressures at 5 K. The solid lines are obtained by the least-squares calculation for the data.

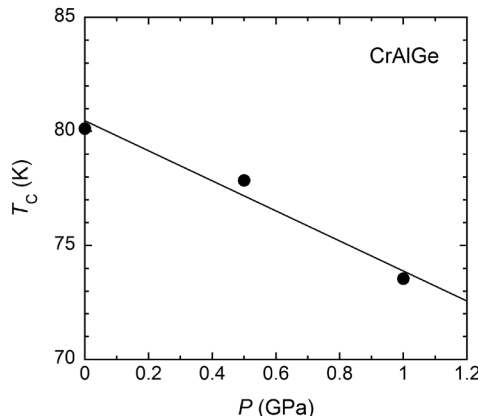


Fig. 2. Pressure dependence of  $T_C$ . The solid line is least-squares fit.

type piston cylinder pressure cell.

Figure 1 shows the isothermal  $M^2$  vs.  $H/M$  plots (Arrott plots) at 5 K under several  $P$ .  $p_s$  at 0.1 MPa was determined to be  $0.41 \mu_B/\text{f.u.}$  With increasing  $P$ ,  $p_s$  decreased, and  $d\ln p_s/dP$  was  $-9.5 \times 10^{-5} / \text{MPa}$ . Fig. 2 shows  $P$  dependence of  $T_C$ . With increasing  $P$ ,  $T_C$  decreased, and  $d\ln T_C/dP$  was  $-8.2 \times 10^{-5} / \text{MPa}$ . This is probably due to the increase of the 3d-bandwidth and the density of states in the vicinity of the Fermi level.

#### References

- [1] S. Yoshinaga, *et al.*, Physics Procedia **75**, 918 (2015).
- [2] Y. Takahashi, J. Phys.: Condens. Matter. **13**, 6323 (2001).

#### Authors

S. Yoshinaga<sup>a</sup>, Y. Mitsui<sup>a</sup>, R.Y. Umetsu<sup>b</sup>, Y. Uwatoko, and K. Koyama<sup>a</sup>  
<sup>a</sup>Kagoshima University  
<sup>b</sup>Tohoku University

## Development of Cantilever Magnetometry Technique for Organic Samples and Its Application to TPP[Mn(Pc)(CN)<sub>2</sub>]<sub>2</sub>

K. Torizuka, H. Tajima, and Y. Uwatoko

We have developed the cantilever magnetometry technique to investigate magnetic properties of organic samples. A commercially available microcantilever for the atomic force microscopy (AFM) was employed. As shown in Fig. 1, our sample was situated at the tip of the cantilever

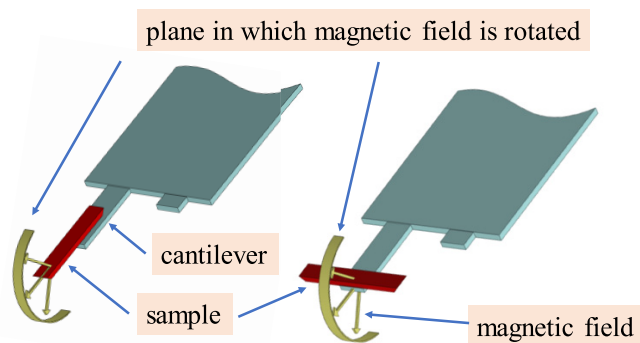


Fig. 1. Sample setup.

beam, depending on the plane in which the magnetic field is rotated. The experimental cell in which the sample was mounted was cooled by a <sup>3</sup>He refrigerator in a superconducting split-type magnet. The field direction is horizontal and the maximum field strength is 7 T. The magnet can be rotated so that the magnetic field direction can be changed by 360 degrees in a plane perpendicular to a vertical axis.

For the electrical circuit, two piezoresistors and two metal film resistors ( $47 \text{ k}\Omega$ ) constituted a Wheatstone bridge. The signal which comes out from the electrical circuit is expressed by the quantity,  $x \approx \Delta R/R_{\text{ref}}$  ( $\Delta R \equiv R_{\text{ref}} - R_{\text{cant}}$ , where  $R_{\text{ref}}$  and  $R_{\text{cant}}$  are piezoresistivities of the reference and the cantilever). This quantity  $x$  is proportional to the torque when  $x$  is small, but changes nonlinearly as  $x$  becomes larger [1].

The advantage of this technique is that even if the sample is very tiny, we can obtain the torque signal. In fact, the mass of our sample is approximately  $1 \mu\text{g}$ . This technique is a very sensitive one.

We carried out magnetic torque measurements for TPP[Mn(Pc)(CN)<sub>2</sub>]<sub>2</sub>, that is isostructural to TPP[Fe(Pc)(CN)<sub>2</sub>]<sub>2</sub>. The latter is a well-known molecular conductor showing the negative giant magnetoresistance. Our motivation is to clarify the magnetic structure for the former sample. The sample has d<sup>4</sup> electrons which behave as a localized magnetic moment with spin  $S = 1$ .

The angular dependence of the torque when the magnetic field is rotated in a plane including  $c$ -axis is depicted in Fig. 2. The data shows a two-fold symmetry reflecting the crystal structure. The d electron emerges in the curve, which is characteristic for the ferromagnetism. However, since the susceptibility data exhibits the antiferromagnetic behavior, d electron should be interpreted as the canting antiferromagnet.

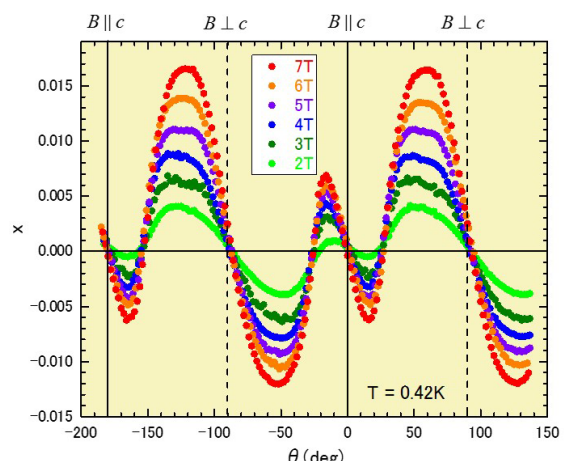


Fig. 2. Torque signal with the field rotated in the plane including  $c$ -axis.

netism [2].

On the other hand, when the magnetic field is rotated in the  $ab$  plane, the torque signal shows a saw-tooth wave form with a four-fold symmetry. It is characteristic for the antiferromagnetic. Considerations on magnetic properties of d electrons as well as  $\pi$  electrons are now in progress.

#### References

- [1] K. Torizuka *et al.*, Jpn. J. Appl. Phys. **52**, 066601 (2013).
- [2] K. Torizuka *et al.*, to be published in J. Phys. Soc. Jpn.

#### Authors

K. Torizuka, H. Tajima<sup>a</sup>, and Y. Uwatoko  
<sup>a</sup>University of Hyogo

## Development of Numerical Library $K\omega$ ver. 1 and Quantum Lattice Solver $H\Phi$ ver. 2

T. Hoshi and Y. Yamaji

The two novel open-source softwares of (i) numerical library  $K\omega$  ver.1 [1] and (ii) quantum lattice solver  $H\Phi$  ver.2 [2] were developed in Project for advancement of software usability in materials science [3] at the fiscal year of 2016. The project name is ‘shifted Krylov-subspace algorithm and novel solvers for computational condensed matter physics’. The project is an interdisciplinary one between computational material science and applied mathematics. The softwares are preinstalled on the supercomputer (sekirei) at ISSP [3]. The two softwares are closely related, because  $K\omega$  is a set of numerical linear-algebraic routines and  $H\Phi$  ver.2 supports the use of  $K\omega$  in the optical spectrum calculations.

$K\omega$  is a general numerical library for the Green’s function of  $G_{ab}(\omega) = \langle a | [(E_0 + \omega + i\delta)I - H]^{-1} | b \rangle$ , where  $H$  is a large scale complex Hermitian or real-symmetric matrix and  $|a\rangle$ ,  $|b\rangle$  are the input vectors. Traditionally, the problem was solved by the Lanczos-based algorithm. In the present solver, instead, the numerical solution is obtained from the linear equation of  $[(E_0 + \omega + i\delta)I - H] |x\rangle = |b\rangle$  and the solution of  $|x\rangle$  is obtained by the novel iterative algorithm, called shifted Krylov subspace algorithm [4,5]. The algorithm was used for the excited spectrum of many-body states in a previous paper [5], which motivated us to the present project. The algorithm enables us to control the accuracy of the spectrum  $G_{ab}(\omega)$  at a specific frequency  $\omega$ , when one monitors the residual vector. The method is general and was applied also to many other computational science fields, such as QCD [4], electronic structure calculations, transport calculation with non-equilibrium Green’s function theory.  $K\omega$  is a general numerical library and can be called, in principle, from any material simulator, as well as  $H\Phi$  ver.2. Moreover, a mini application is included in the package of  $K\omega$ , so that

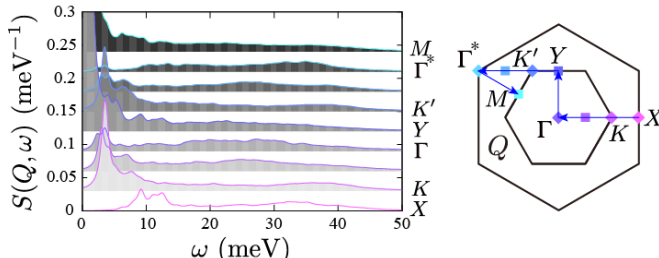


Fig. 1. Calculated dynamical structure factors  $S(Q, \omega)$  of  $\text{Na}_2\text{IrO}_3$  [8]. The spectra are vertically shifted depending on  $Q$ . The Brillouin zone of  $\text{Na}_2\text{IrO}_3$  is shown in the right panel.

researchers can evaluate the numerical library before the use in their real researches.

$H\Phi$  ver. 2 is the latest version of  $H\Phi$  [6]. The quantum lattice solver  $H\Phi$  is a program package based on exact diagonalization applicable to a broad range of quantum lattice models, including the Heisenberg model, the Kitaev model, the Hubbard model and the Kondo-lattice model. In  $H\Phi$  ver. 1, the Lanczos method for calculating the ground state and a few excited states, thermal pure quantum (TPQ) states [7] for finite-temperature calculations, and full diagonalization method for checking results of Lanczos and TPQ methods are implemented with an easy-to-use and flexible user interface. The project in the 2016 fiscal year [3] has supported implementation of the Lanczos and shifted Krylov-subspace algorithm for calculating excitation spectra in the latest version  $H\Phi$  ver.2. The  $H\Phi$  ver.2 call subroutines for the shifted Krylov-subspace algorithm from the library  $K\omega$ .

As an example tractable by  $H\Phi$  ver.2, we show excitation spectra of an ab initio spin hamiltonian of an iridium oxides  $\text{Na}_2\text{IrO}_3$  [8], which is a so-called Kitaev material and a typical example of frustrated magnets due to magnetic anisotropy. In Fig.1, dynamical spin structure factors calculated for a 24-site cluster of the ab initio spin hamiltonian of an iridium oxides  $\text{Na}_2\text{IrO}_3$  are shown. The continuum in the spectra is the hallmark of the proximity to the Kitaev’s quantum spin liquid. The controlled accuracy of the shifted Krylov-subspace algorithm safely resolves the detailed continuum spread over the wide range of frequency, where the typical exchange energy scale of  $\text{Na}_2\text{IrO}_3$  is 30 meV.

#### References

- [1] <https://github.com/issp-center-dev/Komega>
- [2] <https://github.com/QLMS/HPhi>
- [3] <http://www.issp.u-tokyo.ac.jp/supercom/softwaredev>
- [4] A. Frommer, BiCGStab( $l$ ) for families of shifted linear systems, Computing **70**, 87 (2003).
- [5] S. Yamamoto, T. Sogabe, T. Hoshi, S.-L. Zhang and T. Fujiwara, J. Phys. Soc. Jpn. **77**, 114713 (2008).
- [6] M. Kawamura, K. Yoshimi, T. Misawa, Y. Yamaji, S. Todo, N. Kawashima, Computer Physics Communications (to be published).
- [7] S. Sugiura and A. Shimizu, Phys. Rev. Lett. **108**, 240401 (2012).
- [8] Y. Yamaji, Y. Nomura, M. Kurita, R. Arita, and M. Imada, Phys. Rev. Lett. **113**, 107201 (2014).

#### Authors

T. Hoshi<sup>a</sup>, Y. Yamaji<sup>b</sup>, M. Kawamura, K. Yoshimi, T. Misawa, S. Todo<sup>b</sup>, T. Sogabe<sup>c</sup>, and N. Kawashima  
<sup>a</sup>Tottori University  
<sup>b</sup>The University of Tokyo  
<sup>c</sup>Nagoya University

## Structural Characterization of Module-Assembled Amphiphilic Conetwork Gels

M. Shibayama, S. Kondo, and E. P. Gilbert

Amphiphilic conetworks are composed of hydrophilic and hydrophobic polymers. Their amphiphilicity is promising for many applications because amphiphilic conetworks can absorb both polar and nonpolar solutes. This is useful for drug delivery, drug release systems, antifouling coatings, gas and biosensors, chiral separation membranes, activating carriers for biocatalysts, and soft contact lenses. We developed inhomogeneity-free amphiphilic conetworks consisting of poly(ethylene glycol)-poly(dimethylsiloxane) (PEG-PDMS) and carried out structural analysis by the complementary use of small-angle X-ray (SAXS) and neutron scattering (SANS). Figure 1 shows the preparation

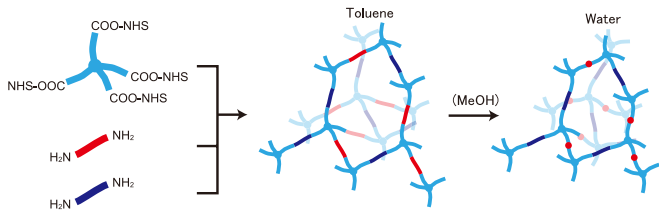


Fig. 1. Schematics of sample preparation for PEG–PDMS gels with  $r = 0.5$ . Light blue, dark blue, and red segments represent tetra-arm-PEG, linear-PEG, and linear-PDMS units, respectively. In toluene, the gels are in swollen state, while they undergo microphase separation in water due to shrinking of the PDMS chains.

scheme of PEG–PDMS gels. The main components were two types of tetra-arm PEGs; –COO-NHS terminated PEG (NHS: N-hydroxysuccinimide) and –NH<sub>2</sub> terminated PEG. In addition, the weight fraction of PDMS in the conetworks,  $r$ , was tuned by using –NH<sub>2</sub> terminated linear-PEG. By using equimolar prepolymers carrying –COO-NHS and –NH<sub>2</sub>, a precise tuning of PDMS content rate was achieved. Because of the hydrophobicity of PDMS units, the PEG–PDMS gels exhibit a microphase-separated structure in water. Figure 2 shows the SANS profiles of swollen PEG–PDMS gels with various solvents. The SANS profiles exhibited marked changes depending on the solvent; from a monotonous decrease without peak for toluene to multiple peaks for water.

Depending on the volume fraction of PDMS, the microphase-separated structure varies from core–shell to lamellar. The obtained SAXS and SANS profiles are reproduced well using a core–shell model together with a Percus–Yevick structure factor when the volume fraction of PDMS is small. The domain size is much larger than the size of individual PEG and PDMS unit, and this is explained using the theory of block copolymers. Reflecting the homogeneous dispersion conditions in the as-prepared state, scattering peaks are observed even at a very low PDMS volume fraction (0.2%). When the volume fraction of PDMS is large, the microphase-separated structure is lamellar and is demonstrated to be kinetically controlled by nonequilibrium and topological effects. The microphase separation in the PEG–PDMS gels is illustrated schematically in Figure 3. It is clarified that the microphase-separated structure is tunable by changing the molecular weight of PEG and PDMS and their proportion. This may open the door for the precise design of the mesoscopic structure of amphiphilic gels.

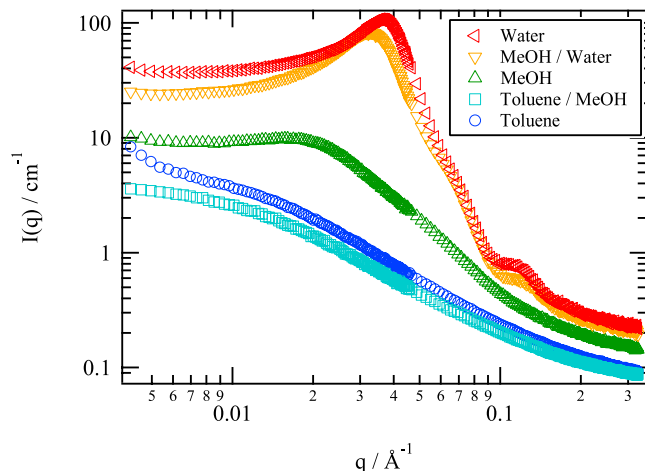


Fig. 2. SANS profiles of PEG–PDMS gels ( $r = 1$ ) with different solvents. The ratios of toluene/MeOH and MeOH/water are both 1/1 (volume fraction). By decreasing the solubility of PDMS, the gels undergo microphase separation, giving rise to distinct peaks in SANS.

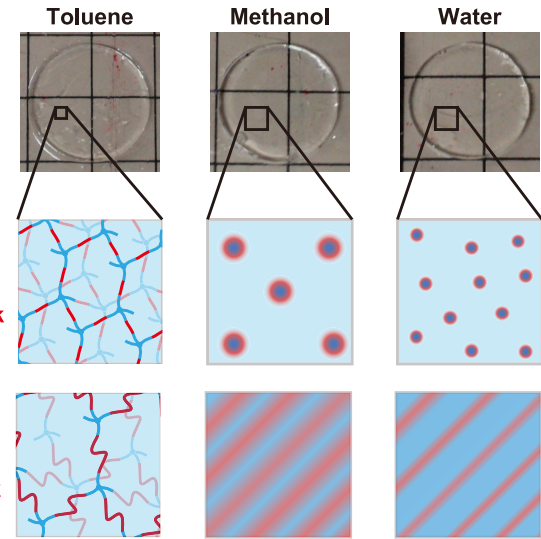


Fig. 3. Proposed phase separation mechanism during solvent substitution from toluene, methanol, to water. The morphology is dependent on the ratio of PEG and PDMS as well as their molecular weights.

#### Reference

- [1] T. Hiroi, S. Kondo, T. Sakai, E. P. Gilbert, Y. S. Han, T. H. Kim, and M. Shibayama, *Macromolecules* **49**, 4940 (2016).

#### Authors

T. Hiroi, S. Kondo<sup>a</sup>, T. Sakai<sup>a</sup>, E. P. Gilbert<sup>b</sup>, Y. S. Han<sup>c</sup>, T. H. Kim<sup>c</sup>, and M. Shibayama<sup>a</sup>

<sup>a</sup>The University of Tokyo

<sup>b</sup>Australian Nuclear Science and Technology Organization

<sup>c</sup>Korea Atomic Energy Research Institute

## Magnetoelectric Behavior in a Chiral Antiferromagnet Ba(TiO)Cu<sub>4</sub>(PO<sub>4</sub>)<sub>4</sub>

Y. Kato, K. Kimura, and A. Miyake

A unique asymmetric magnetic unit, square cupola (see Fig. 1), has been realized in newly synthesized magnetoelectric compounds,  $A(\text{TiO})\text{Cu}_4(\text{PO}_4)_4$  ( $A = \text{Ba}, \text{Sr}$ ) [1]. Spatial asymmetry often activates the asymmetric interactions between localized spins through the relativistic spin-orbit coupling, e.g., the Dzyaloshinskii-Moriya (DM) interaction. The asymmetric interactions lead to intriguing magnetism such as spin-spiral orderings and skyrmion crystals. They have attracted growing interest as an origin of unusual magnetic and electronic properties, such as the magnetoelectric (ME) effect, that is cross-correlations between magnetism and dielectricity. The compound  $\text{Ba}(\text{TiO})\text{Cu}_4(\text{PO}_4)_4$  indeed exhibits a divergent anomaly of the dielectric constant at the Néel temperature ( $T_N = 9.5$  K) [2].

Here we report the ME properties of this compound

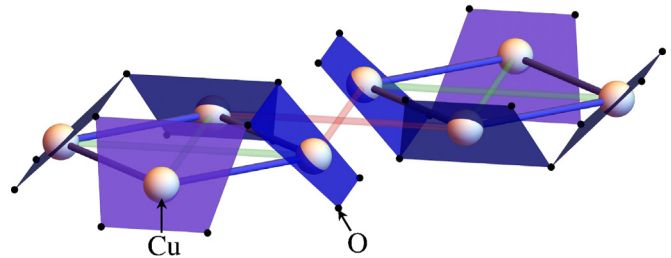


Fig. 1. Square cupolas made of  $\text{Cu}_4\text{O}_{12}$  in  $A(\text{TiO})\text{Cu}_4(\text{PO}_4)_4$  ( $A = \text{Ba}, \text{Sr}$ ). The materials have a quasi-two-dimensional structure, composed of an alternating array of upward and downward Cu-cupolas.

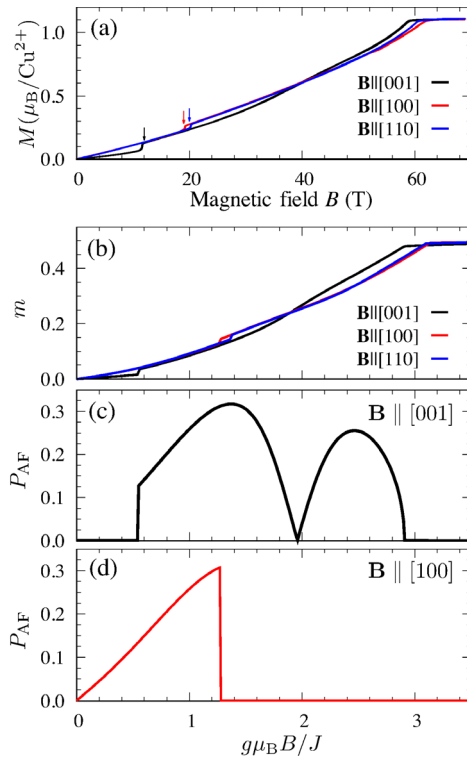


Fig. 2. (a) Magnetization curves in the experiment at  $T = 1.4$  K. The arrows indicate the jump-like anomalies. (b) Magnetization curves of the minimal theoretical model obtained by the cluster mean-field approach. (c,d) Magnetic field dependence of the anti-ferroelectric polarization ( $P_{AF}$ ) for (c)  $\mathbf{B} \parallel [001]$  and (d)  $\mathbf{B} \parallel [100]$ . The electric polarization is computed based on the exchange striction mechanism. All the data are taken from Ref. [3].

by a combined experimental and theoretical study [3]. The magnetization is measured up to the external magnetic field above the saturation at the temperature far below  $T_N$  ( $T = 1.4$  K) at the International MegaGauss Science Laboratory of the Institute for Solid State Physics at the University of Tokyo. As shown in Fig. 2(a), the magnetization curves exhibit the field-direction dependence with several jump-like anomalies, indicating the importance of the spin-orbit coupling. For understanding the unusual behavior, we construct a minimal theoretical model and study the ground-state and finite-temperature properties of the model. In the compound, because of the loss of inversion symmetry at the centers of bonds connecting the nearest neighbor Cu cations having  $S = 1/2$  degrees of freedom, the DM interaction between the nearest neighbor spins is activated. Taking into account the DM interaction in the model and solving it by the cluster mean-field approximation, we successfully reproduce the entire magnetization curves, as shown in Fig. 2(b), especially, the directional dependence of the saturation fields and the critical fields of the jump-like anomalies. We show that the anomalies are explained by ME phase transitions associated with the noncollinear antiferromagnetic ordering and the antiferroelectric ordering. (See Figs. 2(c) and 2(d).) Moreover, our theory also explains the scaling of the dielectric anomaly at the Néel temperature observed in the experiments.

By further analysis of the model, we elaborate the ME phase diagram of the model by changing the magnetic field and the temperature. The results clarify the crucial role of the in-plane component of the DM vector. We also predict a “hidden” phase and ME response in a nonzero magnetic field, both of which await the experimental confirmation. Our results demonstrate how the asymmetric magnetic units activate the ME responses through the DM interactions

arising from the spin-orbit coupling. The present study could inspire motivation on the material design for ME-active materials composed of such asymmetric units.

## References

- [1] K. Kimura, M. Sera, and T. Kimura, *Inorg. Chem.* **55**, 1002 (2016).
- [2] K. Kimura, P. Babkevich, M. Sera, M. Toyoda, K. Yamauchi, G. S. Tucker, J. Martius, T. Fennell, P. Manuel, D. D. Khalyavin *et al.*, *Nat. Commun.* **7**, 13039 (2016).
- [3] Y. Kato, K. Kimura, A. Miyake, M. Tokunaga, A. Matsuo, K. Kindo, M. Akaki, M. Hagiwara, M. Sera, T. Kimura, and Y. Motome, *Phys. Rev. Lett.* **118**, 107601 (2017).

## Authors

Y. Kato<sup>a</sup>, K. Kimura<sup>b</sup>, A. Miyake, T. Kimura<sup>b</sup>, M. Hagiwara<sup>b</sup>,

M. Tokunaga, K. Kindo, and Y. Motome<sup>a</sup>

<sup>a</sup>The University of Tokyo

<sup>b</sup>Osaka University

## Evidence of Charge Transfer and Orbital Magnetic Moment in the Multiferroic CuFeO<sub>2</sub>

Y. Narumi, T. Nakamura, and H. Ikeda

Original meaning of “multiferroics” is coexistence of “multiple” and “ferroic” ordered states. However, nowadays, multiferroics is commonly recognized as phenomena involving antiferroic properties such as antiferromagnetic. As a result, multiferroics comes to have diversity in functionality, such as magnetic-field-control of ferroelectricity. The triangular lattice antiferromagnet CuFeO<sub>2</sub> (abbreviated to CFO) shows ferroelectricity in a finite magnetic field [1]. Nominal oxidation state of Fe is Fe<sup>3+</sup> ( $3d^5$ ) with spin  $S = 5/2$  and with orbital singlet  $L = 0$ . Therefore a classical ordered state is expected to be a noncollinear 120 degrees spin arrangement. However, in reality, CFO shows a 4-sublattice collinear magnetic ordering below 11 K by forming a scalene triangle, because of the geometrical frustration and a spin-lattice coupling. By an application of magnetic field, CFO shows successive magnetization jumps, although no magnetic anisotropy is expected. The ferroelectricity can be explained by a recently proposed mechanism, *d-p* hybridization, in which a spin-dependent charge transfer (CT) between the transition metal and the ligand is essential [2].

The aim of the present study is to clarify the local electronic state of CFO, which should play an important role

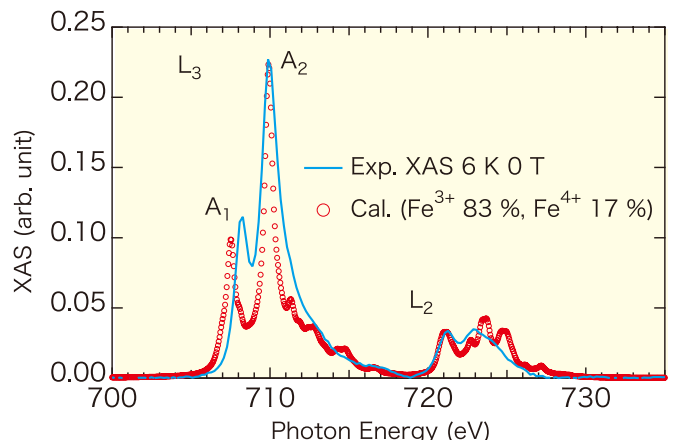


Fig. 1. Experimental (blue solid line) and theoretical (red open circle) XAS's of Fe  $L_{2,3}$ -edge of CFO at 6 K without magnetic field. The data are offset and amplified by a numerical factor so as to scale them at the pre-edge and the maximum of  $L_3$ -edge.

in the ferroelectricity and the magnetic anisotropy. For that reason, we performed x-ray magnetic circular dichroism (XMCD) measurements in high magnetic fields at SPring-8/BL25SU [3]. By tuning an incident energy to the absorption edge of a specific magnetic ion, XMCD gives us the spin and orbital magnetic moments of the ions independently. Moreover the x-ray absorption spectrum (XAS) is sensitive to the valence state of the ion. Therefore we are able to investigate both magnetic and electronic properties from the microscopic point of view. The ultra-high vacuum chamber equipped with a pulse magnet was developed in collaboration with Tohoku University, SPring-8, and University of Tokyo. This is the unique soft x-ray spectrometer reaching 40 T in the world.

Figure 1 shows the comparison between the experimental XAS of Fe  $L_{2,3}$ -edge at 6 K and the ab-initio multiplet calculation at 0 T. The broadness of the experimental XAS is not due to resolution. It is because that there is a restriction of the number of the electronic configurations in the calculations. There is unignorable discrepancy with respect to the energy split between main  $A_2$  and satellite  $A_1$  peaks. This is also due to the same reason as the fine structures in the theoretical calculation. Although nominal valence of Fe is  $\text{Fe}^{3+}$ , an addition of a small amount of  $\text{Fe}^{4+}$  component leads to a better agreement than the theoretical XAS of only  $\text{Fe}^{3+}$ . Figure 2 represents experimental results of Fe  $L_{2,3}$ -edge XMCD at 15.1 T and corresponding energy-integral. By analysis based on sum rule, the ratio of spin ( $m_s$ ) to orbital ( $m_o$ ) magnetic moments was determined to be  $m_s/m_o = -0.071$ . That is, the  $m_s$  and  $m_o$  point in the opposite direction to each other.

According to Hund's rules, the antiparallel configuration of the  $m_s$  and  $m_o$  leads to the fact that the 3d electronic configuration of Fe should be less than half-filled. In other words, we can say that  $\text{Fe}^{4+}$  ( $3d^4$ ) state exists. From the viewpoint of charge compensation among ions, presence of  $\text{Fe}^{4+}$  ion needs a CT from somewhere. Accordingly, we measured XAS of Cu  $L_{2,3}$ -edges and related compounds for comparison. Surprisingly, it turned out that the valence state of Cu is similar to neither that of  $\text{Cu}^+$  nor that of  $\text{Cu}^{2+}$ , but that of Cu metal. This gives a new insight that it is important to take into consideration for correlation between Fe and Cu as well as oxygen in order to fully understand ferroelectric and magnetic properties of CFO.

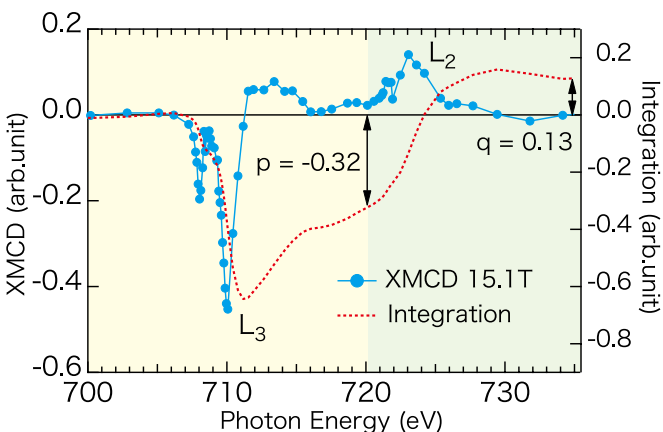


Fig. 2. Experimental XMCD of Fe  $L_{2,3}$ -edges at 15.1 T (blue solid line with solid circle) and integration of it (red dashed line). According to Sum rule, the ratio of spin to orbital magnetic moments is given by  $m_s/m_o = 2q/(9p - 6q)$ . The numerical values of  $p$  and  $q$  indicated by arrows are the integrals of the XMCD over the  $L_3$  and the whole  $L_{2,3}$  absorption regions, respectively.

## References

- [1] T. Kimura, *et al.*, Phys. Rev. B **73**, 220401(R) (2006).
- [2] T. Arima, J. Phys. Soc. Jpn. **76**, 073702 (2007).
- [3] Y. Narumi, *et al.*, J. Phys. Soc. Jpn. **85**, 114705 (2016).

## Authors

- Y. Narumi<sup>a</sup>, T. Nakamura<sup>b</sup>, H. Ikeno<sup>c</sup>, N. Terada<sup>d</sup>, T. Morioka<sup>a</sup>, K. Saito<sup>a</sup>, H. Kitazawa<sup>d</sup>, K. Kindo, and H. Nojiri<sup>a</sup>  
<sup>a</sup>Tohoku University  
<sup>b</sup>SPring-8  
<sup>c</sup>Osaka Prefecture University  
<sup>d</sup>National Institute for Materials Science

## High-field Magnetization Study of the $S = 1/2$ Kagome Lattice Antiferromagnet $\text{CaCu}_3(\text{OH})_6\text{Cl}_2 \cdot 0.6\text{H}_2\text{O}$

H. Yoshida, Y. Narumi, and M. Hagiwara

Seeking the quantum spin liquid state has been one of the central issues of the condensed matter physics. Various theories expected to realize the quantum spin liquid state on the Kagome lattice antiferromagnet owing to the strong frustration and the quantum fluctuation. Recently, the appearance of non-trivial magnetization plateaus at  $(2n + 1)M_s/9$  for the  $S = 1/2$  Kagome lattice antiferromagnet was predicted by the grand canonical DMRG [1] and Tensor network method [2], and thus the study of the magnetization curves of the Kagome lattice antiferromagnet has been of significant interest. However, the lack of appropriate model compounds is one of the difficulties to understand the magnetic properties of Kagome lattice antiferromagnet in the high magnetic fields.

Recently, we have succeeded to prepare the single crystal of  $S = 1/2$  Kagome lattice antiferromagnet  $\text{CaCu}_3(\text{OH})_6\text{Cl}_2 \cdot 0.6\text{H}_2\text{O}$  which has the perfect Kagome lattice without an anti-site disorder [3]. This compound possesses magnetic interactions of the nearest neighbor interaction  $J_1$ , and the next nearest neighbor  $J_2$ , and the  $J_d$  across the hexagon as shown in the inset of Fig. 1. Thus, an emergence of a novel magnetic state on the Kagome lattice is expected by the competition of the magnetic interactions. In this study, we report on magnetic properties of the single crystal of  $\text{CaCu}_3(\text{OH})_6\text{Cl}_2 \cdot 0.6\text{H}_2\text{O}$  revealed by the magnetic susceptibility, heat capacity, and high-field magnetization measurements [3].

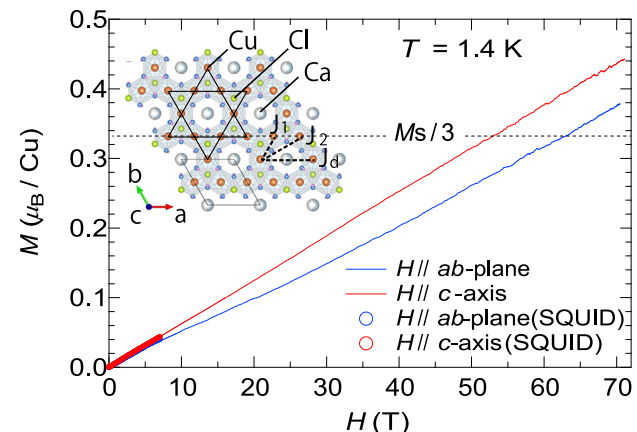


Fig. 1. The magnetization curves measured on the single crystal of  $\text{CaCu}_3(\text{OH})_6\text{Cl}_2 \cdot 0.6\text{H}_2\text{O}$  at 1.4 K up to the magnetic field of 71 T. The dashed line is the guide to the eye for the  $1/3$  magnetization of the saturation moment of  $S = 1/2$ . The inset shows the schematic illustration of the Kagome layer of  $\text{CaCu}_3(\text{OH})_6\text{Cl}_2 \cdot 0.6\text{H}_2\text{O}$  with the magnetic interactions  $J_1$ ,  $J_2$ , and  $J_d$ .

The magnetic interactions of antiferromagnetic  $J_1 = 52.2$  K,  $J_d = 11.9$  K, and ferromagnetic  $J_2 = -6.9$  K were extracted from the 9th order high temperature series expansion analysis. The magnetic susceptibility and the heat capacity measurements indicated that an occurrence of an unusual magnetic transition at  $T^* = 7.2$  K where only the  $\chi_{ab}$  showed the cusp and the heat capacity exhibited the tiny peak anomaly. The cusp in the  $\chi_{ab}$  disappeared above around 5 T, and it exhibited temperature independent behavior below  $T^*$ . Remarkably, in spite of the fact that the compound is an insulator, the temperature-linear term  $5.9 \text{ mJ/CumolK}^2$  at  $H = 0$  T was observed in the heat capacity which was suppressed by the magnetic field around 10 T. This suggests that the unconventional magnetic excitation underlies on the ground state of  $\text{CaCu}_3(\text{OH})_6\text{Cl}_2 \cdot 0.6\text{H}_2\text{O}$  [3].

Figure 1 shows the magnetization curves for both  $H \parallel ab$ -plane and  $H \parallel c$ -axis at 1.4 K up to 71 T. The magnetization along the  $c$ -axis increases monotonously. In contrast, a slope of the curve for  $H \parallel ab$ -plane becomes small above 5 T which may correspond to the disappearing of the cusp in  $\chi_{ab}$  and the  $T$ -linear term in the magnetic field, and one can clearly see the upward convex feature above the 5 T anomaly. No meta-magnetic transitions and magnetization plateau at  $M_s/9$  and  $M_s/3$  for both directions were found. This may be attributed to the effect of the magnetic interactions  $J_2$  and  $J_d$  which has not been considered in the theoretical calculations[1,2]. In order to clarify the magnetic properties of the  $S = 1/2$  ideal Kagome lattice antiferromagnet, the magnetization measurement in the much higher field, microscopic measurements such as high-field ESR and theoretical investigation are required.

#### References

- [1] S. Nishimoto *et al.*, Nature Commun., **4**, 2287 (2013).
- [2] T. Picot *et al.*, Phys. Rev. B, **93**, 060407(R) (2016).
- [3] H. Yoshida *et al.*, J. Phys. Soc. Jpn., **86**, 033704 (2017).

#### Authors

H. Yoshida<sup>a</sup>, N. Noguchi<sup>a</sup>, M. Oda<sup>a</sup>, T. Kida<sup>b</sup>, Y. Narumi<sup>b</sup>, and M. Hagiwara<sup>a</sup>  
<sup>a</sup>Hokkaido University  
<sup>b</sup>Osaka University

## A Compact Permanent-Magnet System for Measuring Magnetic Circular Dichroism in Resonant Inelastic Soft X-Ray Scattering

J. Miyawaki, S. Suga, and Y. Harada

Resonant inelastic X-ray scattering (RIXS), especially soft X-ray RIXS (SX-RIXS), has made remarkable progress in energy resolution over the past few decades in conjunction with the improvement of the performance of synchrotron radiation sources and the advancements in the RIXS instrumentation. Accordingly, RIXS has come to occupy an important position in X-ray spectroscopy techniques for investigating the bulk electronic structures. The photon-in/photon-out process adds to RIXS the distinctive feature that the electronic structure can be measured even in an electronic and/or magnetic field. Regarding the use of the magnetic field for RIXS, magnetic circular dichroism (MCD) in RIXS (RIXS-MCD) has intensively been used to extract spin-resolved valence band excitations. In addition to all the features inherited from RIXS itself, RIXS-MCD of  $dd$  excitations that can easily be separated by the use of the latest

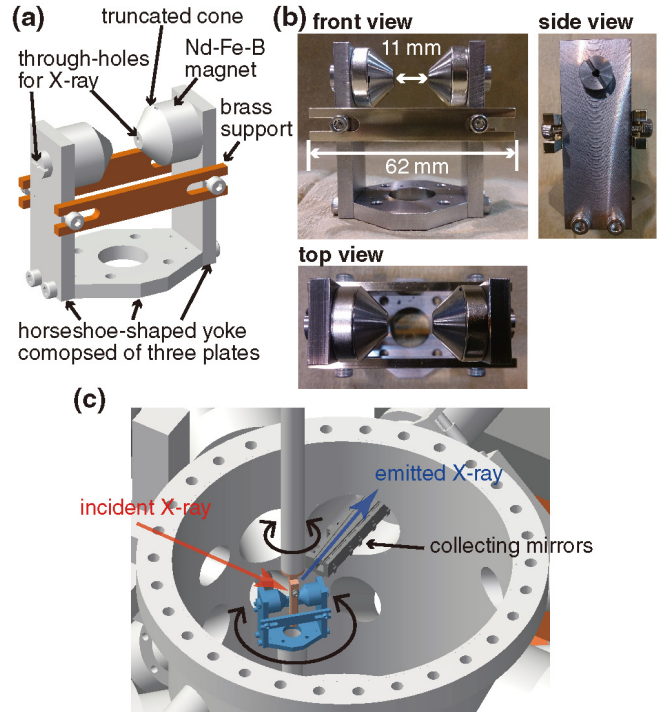
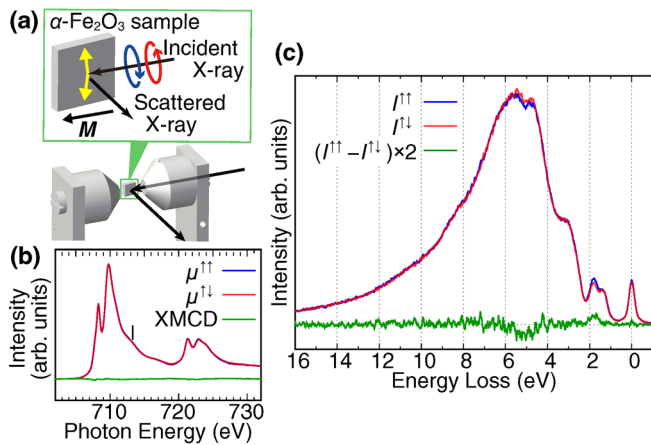


Fig. 1. Schematic representation and photographs of the magnet system and experimental setup. (a) Schematic representation and (b) photographs of the magnetic circuit. The magnets are fixed by a screw with a through-hole for the X-ray beam. (c) Experimental configuration of RIXS-MCD at the HORNET end-station in SPring-8 BL07LSU when the angle of the magnetic field is set at  $45^\circ$  to the incident X-ray.

high-energy-resolution RIXS apparatus can provide magnetic information for each localized  $d$  orbital. With these advantages, RIXS-MCD is becoming a very promising technique, and is expected to be successfully applied to new functional materials in which spins play important roles, such as multi-ferroics and those to be used for spintronic devices. In order to demonstrate the significance of RIXS-MCD with high energy resolution and encourage its wider use, it is highly desired that RIXS-MCD experiments can be performed as a common tool at any RIXS end-station in worldwide synchrotron radiation facilities. Therefore, we developed a compact and portable magnet system for RIXS-MCD composed of Nd-Fe-B permanent magnets which can generate a magnetic field of  $\sim 0.25$  T [1].

Figures 1(a) and 1(b) display a schematic drawing and photographs of the originally-designed magnetic circuit. The magnetic circuit consists of Nd-Fe-B magnets, a horseshoe-shaped yoke, truncated cone poles, and two supports. The Nd-Fe-B magnets are the source of the magnetic field. The horseshoe-shaped yoke and truncated cone poles are made of Fe, and functions to focus the magnetic fields. The two supports are made of brass, and function to resist the attractive force between the magnets. The overall size of the magnetic circuit is within  $\varnothing 65$  mm so that it can be installed through and mounted on the most commonly used 4-1/2 inch-diameter ConFlat® flange. This compact design of the magnetic circuit allows it to be installed without any modification to the existing vacuum chambers and optical systems for RIXS. Figure 1(c) is a schematic representation of the experimental configuration in a vacuum chamber using this magnet system at the HORNET end-station in SPring-8 BL07LSU.

We have demonstrated the capability of the present magnet system for RIXS-MCD. Figure 2 shows X-ray magnetic circular dichroism (XMCD) and RIXS-MCD of



**Fig. 2.** Fe  $L$ -edge XMCD and RIXS-MCD spectra of an  $\alpha\text{-Fe}_2\text{O}_3(111)$  single crystal. (a) Sketch of the experimental configuration with the orientation of the spin. The magnetic field is parallel to the incident X-ray and the incident angle is  $10^\circ$  from the sample surface. Yellow arrows on the  $\alpha\text{-Fe}_2\text{O}_3(111)$  sample represent the direction of the antiferromagnetically coupled and canted spin moments on the (111) plane. (b) Fe  $L_{2,3}$ -edge XAS spectra measured by circularly polarized X-rays with the XMCD spectrum. (c) RIXS-MCD spectra measured at  $h\nu = 713.25$  eV indicated by a vertical line in (b).

weak ferromagnetism in  $\alpha\text{-Fe}_2\text{O}_3$ . We measured XMCD and RIXS-MCD in the grazing incidence geometry as shown in Fig. 2(a). No discernible signal was detected in its XMCD spectrum [Fig. 2(b)]. This is because the net magnetic moment owing to the weak ferromagnetism is too small to be detected. Figure 2(c) exhibits the RIXS-MCD spectra excited at the charge-transfer satellite as indicated by the solid line in Fig. 2(b). RIXS-MCD was clearly observed at 1.8 and 4.85 eV loss energies, which are assigned to a  $dd$  excitation and a charge-transfer transition, respectively. Thus, RIXS-MCD was clearly observed by high-energy-resolution RIXS, though XMCD was not observed. These results confirmed that the observed RIXS-MCD was induced by the RIXS process, via the different relaxation probabilities of polarized valence electrons to polarized core holes created by the circularly polarized X-rays. These results suggest that more useful bulk information about the ground-state spin state can be obtained by using RIXS-MCD.

#### Reference

- [1] J. Miyawaki, S. Suga, H. Fujiwara, H. Niwa, H. Kiuchi, and Y. Harada, *J. Synchrotron Rad.* **24**, 449 (2017).

#### Authors

- J. Miyawaki, S. Suga<sup>a</sup>, H. Fujiwara<sup>a</sup>, H. Niwa, H. Kiuchi, and Y. Harada  
<sup>a</sup>Osaka University

